Guest Entrapment in Metal-Organic Nanosheets for Quantifiably Tuneable Luminescence

Dylan A. Sherman, Mario Gutiérrez, Ian Griffiths, Samraj Mollick, Nader Amin, Abderrazzak Douhal, and Jin-Chong Tan*

Luminescent metal-organic frameworks (LMOFs) are promising materials for nanophotonic applications due to their tuneable structure and programmability. Yet, the 3D nature of LMOFs creates challenges for stability, optical transparency, and device integration. Metal-organic nanosheets (MONs) potentially overcome these limitations by combining the benefits of metal-organic frameworks (MOFs) with an atomically thin morphology of large planar dimensions. Herein, the bottom-up synthesis of few-layer thin ZIF-7-III MONs via facile low-energy salt-templating is reported. Employing guest@MOF design, the fluorophores Rhodamine B and Fluorescein are intercalated into ZIF-7 nanosheets (Z7-NS) to form light emissive systems exhibiting intense and highly photostable fluorescence. Aggregation and Förster resonance energy transfer, enabled by the MON framework, are revealed as the mechanisms behind fluorescence. By varying guest concentration, these mechanisms provide predictable quantified control over emission chromaticity of a dual-guest Z7-NS material and the definition of an "emission chromaticity fingerprint" – a unique subset of the visible spectrum that a material can emit by fluorescence.

1. Introduction

Metal-Organic Framework (MOF) nanosheets, recently termed Metal-Organic Nanosheets (MONs), are an increasingly sought-after form of MOFs that unite the properties of 2D materials with 3D MOF characteristics.[1,2] Nanosheets are high surface-to-volume atom ratio materials with single or few-atom thickness (1–10 nm typically) and comparatively large micron-scale lateral planar dimensions.[3] Archetypal 2D materials, such as MXenes,[4] layered double hydroxides (LDH) and oxides,[5] and graphitic carbon nitrides,[6] have been reduced to nanosheets in multiple studies.[7] These nanosheets have unprecedented physical, electronic, chemical, and optical properties unattainable in their 3D layered bulk counterparts.[7] MONs provide a competitive alternative to these nanosheet materials by adding key MOF characteristics derived from the metal-organic composition. These include structural diversity and tuneability, programmable functionality, mechanical anisotropy,[8,9] and highly ordered pore arrays with abundant accessible active sites.[1] To date, MONs have shown great promise in gas separation and water purification applications,[10,11] energy storage,[12] light harvesting and emission,[1] electronic devices,[13] catalysis,[14,15] and sensing.[16]

ZIF nanosheets are particularly intriguing, given that 3D ZIFs exhibit high stability, hydrophobicity, and large pore size.[17] ZIF-7 [$Zn(bIm)_2$, bIm = benzimidazolate] is isolatable in a dense thermodynamically stable 2D-layered phase ZIF-7-III ($Zn_2(bIm)_4$),[18] making it viable for the formation of nanosheets (**Figure 1**).[19] ZIF-7 nanosheets have been used as a matrix for the ionization of small molecules,[20] molecular sieving,[21] and membranes.[21]

D. A. Sherman, S. Mollick, J.-C. Tan
Multifunctional Materials & Composites (MMC) Laboratory
Department of Engineering Science
University of Oxford
Parks Road, Oxford OX1 3PJ, UK
E-mail: jin-chong.tan@eng.ox.ac.uk

M. Gutiérrez, A. Douhal
Departamento de Química Física
Facultad de Ciencias Ambientales y Bioquímica
INAMOL
Universidad de Castilla-La Mancha
Toledo 45071, Spain
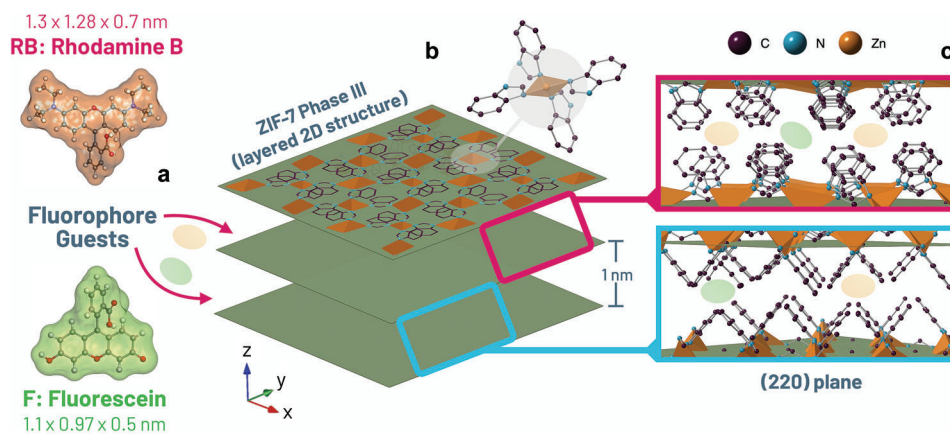E-mail: mario.gutierrez@uclm.es; abderrazzak.douhal@uclm.es

I. Griffiths
Department of Materials
University of Oxford
16 Parks Road, Oxford OX1 3PH, UK

N. Amin
Department of Chemistry
University of Oxford
Mansfield Road, Oxford OX1 3TA, UK

Figure 1. Schematic of material design with structures from single crystal ZIF-7-III data.[33] a) Chemical structures of Rhodamine B and Fluorescein. b) Single secondary building unit with ZnN_4 tetrahedra highlighted on a single sheet (monolayer) of $Zn_2(bIm)_4$ in the *xy*-plane of a segment of ZIF-7-III layered structure with green planes indicating the (002) *d*-spacing. c) Cross section of the (220) plane, illustrating the perpendicular arrangement of layers and interlayer spacing. For all representations: carbon (purple), nitrogen (blue), Zn(II) (orange), oxygen (red), hydrogen (omitted for clarity).

The study of MONs is still in its infancy, with synthesis and stability often the greatest challenges.[3,22] Most studies rely on top-down disassembly of 2D layered MOFs,[23,24] which is energy and time consuming, and typically result in MONs of non-uniform nanosheet dimensions with rough surfaces that commonly reaggregate.[23] Bottom-up synthesis provides greater morphological control and stable isolated sheets, but with few reports in high yield.[14] Examples of bottom-up techniques tailored to specific MOFs, such as ZIF-8 and ZIF-67, include modulation,[25,26] diffusion,[27] surfactant assistance,[28,29] salt-confinement,[30] and interfacial synthesis.[31] To our knowledge, though, there are no reports of ZIF-7-III nanosheet bottom-up synthesis, only top-down delamination.[20,31,32,33] While rarely used for MONs, salt-templating is a frequently cited method of synthesizing nanosheets of 2D materials.[34,35] Acting as a hard-templating agent, salt crystal faces provide an energetically favorable surface for the growth of consistently thin nanosheet materials. Given the ubiquity of NaCl, and ease of its removal via dissolution in H_2O, this method has significant benefits environmentally and for scalability.

One of the lesser explored areas of MONs is luminescent optoelectronics. A fluorescent nano-emitter should have negligible dye leaching, structural stability under ambient conditions and repeated use, and high photoluminescence quantum yield (PLQY). Key to making nano-emitters application-ready is the ability to tune luminescence energetics and chromaticity. Studies have demonstrated that the emission chromaticity of luminescent MOFs (LMOFs) with chromophore guests can be tuned qualitatively by varying the guest loading concentration within the framework pores.[36,37] To our knowledge, however, there is no numerical study of the precise relationship between guest concentration and resulting material luminescence chromaticity. Finding such a correlation would provide unprecedented precision tuneability of luminescence energetics for nano-emitters, a function critical to advancing the field of MON optoelectronics from layered semiconductors to sensors and organic light-emitting diode (OLED) materials.

The majority of LMOF literature targets 3D bulk materials,[38] but these are often unstable in solution due to guest leaching. The host framework can also impede emission via self-quenching, either through energy interconversion and absorption or physical shielding.[39] In contrast, the atomic thickness and increased specific surface area of MONs improve optical transparency, while still allowing strong in-plane covalent bonding for stronger guest binding and chemical stability.[40,41,9] The confinement of electrons in an ultra-thin region also facilitates the control and directionality of excitons emission, which theoretically allows for the optimization of guest luminescence.[42] Exfoliated materials such as AUBM-6-NS, for example, have reported up to threefold greater emission intensity than the bulk AUBM-6.[40]

At present, the overwhelming majority of luminescent MONs (LMONs) utilize inherent luminescence via the design of emissive linkers, metal ions, or via ligand-metal charge transfer.[43] A novel route to LMONs is employing the guest@MOF approach and, to the best of our knowledge, the only work to date considering this approach is the system lanthanide hydrate@MOF nanosheets (HSB-W5-NS).[44] Dyes, alternatively, are ideal for use in guest@MOF systems.[45] Rhodamine B (RB) and Fluorescein (F) (Figure 1a) are two of the most employed guests due to their high PLQY and stability.[46] While F and RB do not fluoresce in solid-state due to aggregation-caused quenching (ACQ),[47,48] isolating monomers via encapsulation in pores of 3D MOFs,[49–52] can induce fluorescence in solid state while also improving long-term guest stability.[53,54] In 3D MOF materials, in situ guest encapsulation strategies are typically employed to overcome small pore apertures prohibiting dye diffusion.[52] In a 2D MON system, we theorize this encapsulation is analogous to intercalation, which has been achieved for RB and F in LDH systems and clays,[55,56] yet the resulting systems are frequently reported as being unstable or lack tuneability.[57,58] The intercalation of organic fluorophores is yet to be explored in MONs, despite the apparent advantages of a more flexible and customizable parent matrix to control loading and tune interlayer spacing.

Herein, we report the first in situ bottom-up synthesis of ultrathin $Zn_2(bIm)_4$ MONs (Z7-NS) via a low-energy and

scalable salt-template synthesis. We show that the fluorescent dyes RB and F can be incorporated into individual Z7-NS using this synthesis to yield highly stable fluorescent guest@MON systems with tuneable emission of visible light. Utilizing nanoscale analysis techniques, we reveal the underpinning mechanisms of guest intercalation. When the dyes are intercalated simultaneously, a dual-guest yellow emitting nano-system results, whose emission chromaticity is precisely tuneable via numerical modelling.

2. Results and Discussion

2.1. Synthesis and Structure of Z7-NS Guest@MON Materials

Z7-NS were synthesized in situ using an environmentally benign salt-templating technique during a one-pot reaction (see Experimental Section). In brief, after coating a large excess of NaCl crystals in $Zn(NO_3)_2$ solution, benzimidazole (bIm) was added with minimal solvent (MeOH) and mixed rapidly to grow Z7-NS. The nanosheets were isolatable by dissolving NaCl in H_2O. Optical microscopy and SEM imaging of a NaCl crystal before synthesis, compared to the reaction mixtures after stirring (Figure S1, Supporting Information), revealed preferential growth of the nanosheets on the surfaces of NaCl crystals, thereby limiting growth along the z-axis. It is well reported that salt particles with large dimensions (such as 20 µm used in this synthesis) and smooth surfaces (see NaCl in Figure S1, Supporting Information) act as this hard template for synthesizing 2D sheets of materials such as metal nitrides and oxides (e.g., MoO_3).[34,35,59] This contrasts with the only reported ZIF nanosheets (ZIF-67) synthesized with salt, which used salt crystals of just 1 µm to grow nanosheets in the voids between salt crystals.[30]

To examine the essential role of the dense NaCl matrix in forming nanosheets, the Z7-NS synthesis was repeated with varied NaCl quantities and compared with ZIF-7-III synthesized using hydrothermal transformation of ZIF-7.[33] All syntheses produced materials with a ZIF-7-III crystal structure, confirmed by PXRD (Figure S2, Supporting Information). The morphology, however, varied progressively with the addition of NaCl. As seen in SEM imaging (Figure S2, Supporting Information), hydrothermal synthesized ZIF-7-III formed layered stacks, while the direct room temperature synthesis without salt produced aggregated layered globules. Synthesis with 0.25x NaCl quantity results in the layered globules beginning to aggregate via interconnected nanosheet layers, similar to the nanosheet networks seen in the reported ZIF-67 salt temptation. At 0.5x NaCl quantity, particles form independently and are predominantly composed of intertwined nanosheets with some remaining globules. This suggests that isolated nanosheets are forming on NaCl surfaces, but the voids in the less dense NaCl crystal confinement likely allow for precursor solution to still concentrate and form stacked materials around the nanosheets. When a large excess of NaCl is used in standard reaction conditions, the void space is filled by the dense NaCl matrix, directing growth preferentially on NaCl surfaces without 3D protrusions.

Fascinatingly, by adding F or RB dissolved in methanol into the synthesis solution, facile in situ guest incorporation into the framework was achieved. Two single-guest systems (F@Z7-NS and RB@Z7-NS) at various guest loadings (guest@Z7-NS-10^{-1},

-10^{-2} and -10^{-3} M using synthesis guest quantities of 0.03, 0.003 and 0.0003 mmol respectively) were formed, along with a dual-guest system (entrapping F and RB simultaneously, DG@Z7-NS). Guest loading was quantified using ^{1}H NMR (see Figure S3 and Table S1, Supporting Information) with data confirming guest loading increases with an increase in guest concentration during synthesis. Synthesis was scalable, tested up to 10 times the initial quantities, producing solid material yields from 93 mg to 1.22 g (70%–80%). Z7-NS remained as stable dispersions in H_2O or MeOH, confirmed by Tyndall scattering (Figure S4, Supporting Information), and are thermally stable up to 550 °C (Figure S5, Supporting Information).

AFM and FE-SEM imaging (**Figure 2**) revealed Z7-NS consistently formed as isolatable few-layer thin nanosheet particles, with this morphology being maintained after the incorporation of guest molecules. The height of over 80 particles per material was determined via individual AFM tomography imaging (Figure 2a,b), with calculated mean heights of 1.9 nm for Z7-NS, 2.6 nm for F@Z7-NS, 2.8 nm for RB@Z7-NS and 3.9 nm for DG@Z7-NS. This height average increase is complementary to the introduction of more bulky guests into the Z7-NS layers, suggesting successful guest incorporation. Height distributions (Figure 2b) and height profiles (Figure 2w) for each material indicate a monolayer of Z7-NS being ≈1.2 nm, with samples preferentially forming in 1–4 layers aggregates dependent on guest (c.f. ZIF-7-III 2D layer stacks of 200 nm average height) (Figure S2, Supporting Information).

AFM height profiles (Figure 2w) along with AFM imaging and FE-SEM (Figure 2c–g for Z7-NS, Figure 2h–l F@Z7-NS, Figure 2m–q for RB@Z7-NS and Figure 2r–v for DG@Z7-NS) indicate nanosheets form mostly as flat plate-like sheets, with occasional curling observed (e.g., Figure 2k–n) that cause concentrated protrusions in AFM surface imaging and 3D particles from thin flat surface-layers of nanosheets observable in SEM (Figure S6, Supporting Information). Similar curling has been observed by silica nanosheets from mechanical strain while mixing during synthesis.[60] AFM phase images (corresponding to the first harmonic of the probe tip's tapping frequency) of select samples imaged in Figure 2 (Figure S7, Supporting Information) highlight the phase homogeneity of imaged nanosheets even with height anomalies on the surface of base nanosheet layers that correspond to potential curling in the z-axis (e.g., Figure 2d). This is in contrast with the distinct phases for Figure 2d and the right particle in Figure 2s, which show contamination on the sample slide. Particles range in size with the smallest lateral dimensions of ≈5×2 µm², average of ≈10×5 µm², and largest of ≈20×10 µm². Fragmentation via the formation of micro-holes was observed in nanosheets ultrasonicated for over 5 min (Figure S8, Supporting Information), suggesting the particle size variations derive from the mixing, purification, and isolation of synthesized materials. Conveniently, the smaller and larger nanosheets were found to be separable by gravitational sedimentation. SEM micrographs of Z7-NS imaged at a 45° tilt highlighted the thinness, curvature, and isolated nature of the nanosheets (Figure S9, Supporting Information). Large-area FE-SEM imaging was collected to confirm consistency with these morphological parameters and homogenous particle dispersion across sample slides, on which they were drop casted for microscopic examinations (Figure S10, Supporting Information). The
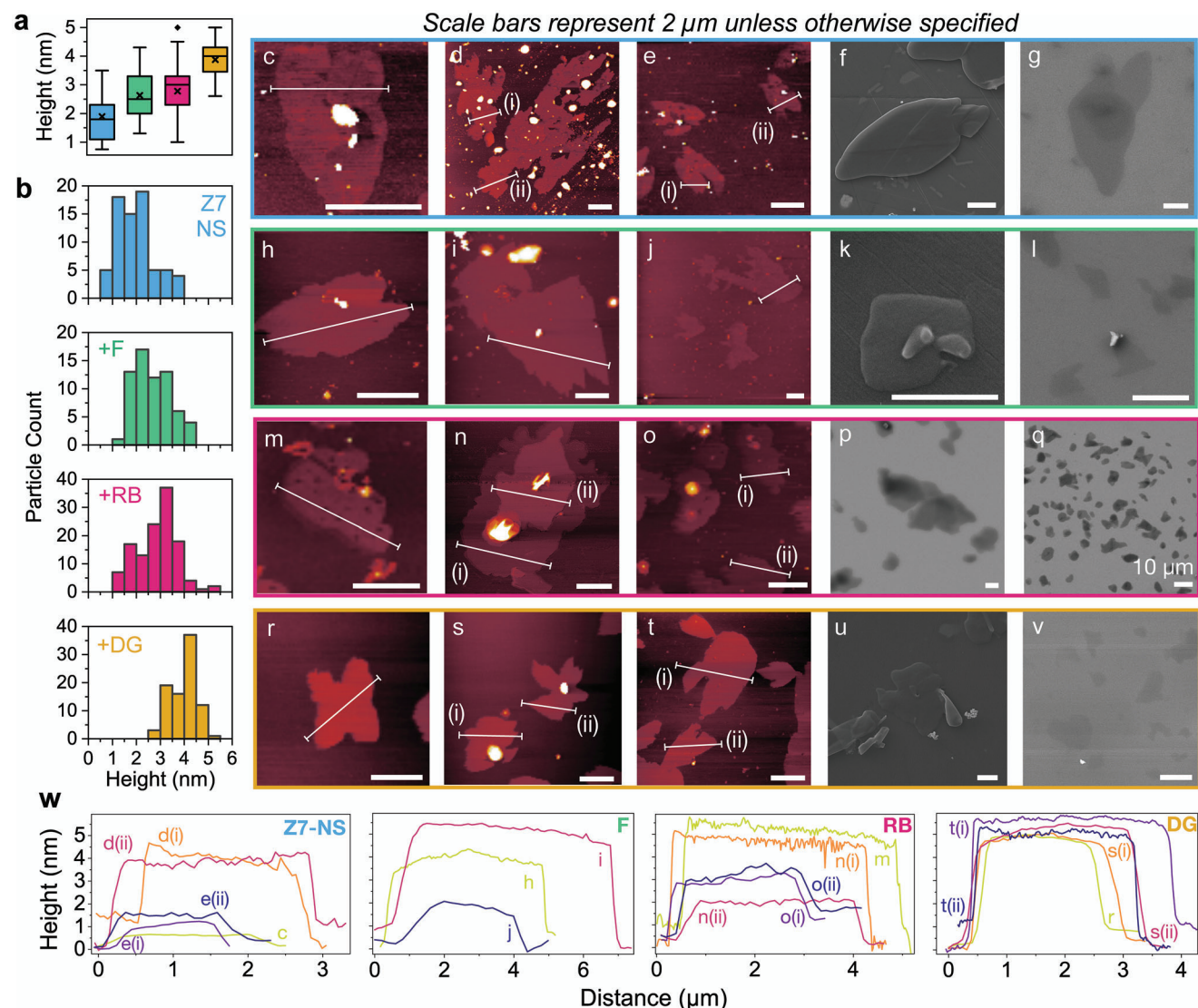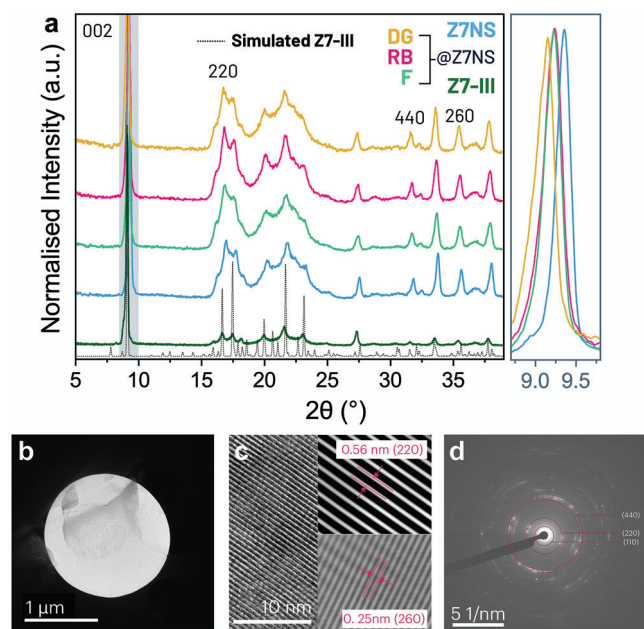
Figure 2. a,b) Heights of over 80 particles of each material (Z7-NS – blue, F@Z7-NS [+F] – green, RB@Z7-NS [+RB] – pink, DG@Z7-NS [+DG] – orange) measured individually using AFM imaging. a) Box plot indicating quartile ranges, median (line), outliers (diamond) and the average height (cross) of each material. b) histogram (0.5 nm bins) height distributions for each material. c–v) AFM surface imaging of material particles on silicon wafer and FE-SEM secondary electron micrographs collected at 10 keV and working distance of 9 mm (samples were either drop-cast onto an aluminium specimen stub and coated with 25 nm of gold [f, k and u], or drop-cast on a silicon wafer [g, l, p-q, v]). Each row is a different material: Z7-NS (c-g), F@Z7-NS (h-l), RB@Z7-NS (m-q) and DG@Z7-NS (r-v). w) Height profiles across select positions in AFM imaging for each material.

morphology remains comparable after 6 months of immersion in water or MeOH, with only slightly increased curling at the nanosheet edges (Figure S11, Supporting Information).

The nanosheet morphology and guest incorporation do not affect the long-range periodicity growth of the host framework, with ZIF-7-III like crystal structure confirmed by direct alignment of PXRD pattern reflections (**Figure 3a**), IR and Raman spectroscopic bands (Figures S12 and S13, Supporting Information). There is no indication of structural transformation or other phase impurities such as NaCl (Figure S14, Supporting Information). Diffraction data further indicate the ultrathin 2D nature of the Z7-NS and the retention of crystallinity across the thin 2D plane. In PXRD patterns (Figure 3a), peak broadening compared to ZIF-7-III and significant reduction in the relative

peak intensity ratio of $I(002)/I(220)$ reflections from 14.814 in ZIF-7-III to 3.941 in Z7-NS indicate reduced diffraction in the z-axis (out-of-plane orientation, see Figure 1b) of the Z7-NS. HR-TEM (Figure 3b,c; Figure S15, Supporting Information) shows large domains of consistent d-spacing across a single nanosheet with an interlayer spacing of 0.56 nm, corresponding to the (220) planes, and 0.25 nm within each of the (220) layers, corresponding to the (260) planes. In the SAED pattern (Figure 3d), three distinctive planes are identifiable upon indexing: the (220) (lowest angle (hkl) reflection with no symmetry about the z-axis), (110) and (440). All three planes have no z-component of symmetry. Thus, we posit the nanosheet has minimal atomic density in the z-axis, while the xy-plane is significantly atomically dense to produce intense diffraction.

**ADVANCED
SCIENCE NEWS**

www.advancedsciencenews.com

**ADVANCED
FUNCTIONAL
MATERIALS**

www.afm-journal.de

Figure 3. a) PXRD patterns of Z7-NS with various dye@Z7-NS. b) TEM image of a single Z7-NS particle studied in (c)-(d). c) Fourier-transform analysed HR-TEM of Z7-NS revealing inter-plane (220) spacing and intra-plane spacing in the (260) plane. d) Selected area electron diffraction (SAED) image of Z7-NS showing indexed planes.

With the ZIF-7 host framework clearly defined, we next considered the location of the guest molecules within the structure. It was not possible to convert the guest@ZIF-7 systems to ZIF-7-III, nor was post-synthesis guest diffusion successful in incorporating guests into ZIF-7-III stacked materials or Z7-NS. Given the molecular dimensions of F and RB ($10.191 \times 9.669 \times 6.43$ Å for F and $13.683 \times 13.233 \times 6.97$ Å for RB),[51] this was expected due to the dense layer packing in ZIF-7-III and limited openings into interlayer spaces. Instead, guests were only incorporable via in situ syntheses, suggesting the guests are in some way being nanoconfined or intercalated within the layered nanosheet system during its formation, rather than merely attached to the external surfaces. Sterically, each guest comprises a xanthene ring with appended phenyl group, known to rotate to a planar conformation in confined spaces (Figure 1a).[61] This, along with their molecular dimensions make the guests feasible to incorporate into the Z7-NS host framework. A single layer of ZIF-7-III comprises of a (4,4) square planar grid formed by corner-sharing networks, quadruply linked, of ZnN_4 tetrahedra (Figure 1b). Each monolayer, of ≈0.5 nm thick, stacks orthogonally rotated on the z-axis via C-H/π interactions, producing 2D channels of ≈1 nm in height through the material's (220) plane (Figure 1c). These channels could accommodate F or RB guests, oriented either perpendicularly or at least inclined at an angle to the layers of Z7-NS. Alternatively, a gap of 0.5 nm between layers provides opportunity for parallel dye encapsulation, with guest phenyl rings able to rest within the pockets between the sterically bulky bIm ligands (these protrude from the Zn centers of each layer but have a degree of rotational flexibility to accommodate guests).

PXRD shows that the (002) d-spacing between nanosheet layers increased following guest intercalation, from 9.44 Å in Z7-

NS to 9.57 Å in F@Z7-NS and RB@Z7-NS, and to 9.66 Å for DG@Z7-NS (Figure 3a). As described earlier, layer height also increased in AFM surface profiles. Vibrational spectroscopy (Raman, MIR and FTIR) revealed no new bands, suggesting no new covalent bonds have formed between the guests and the framework via surface absorption or within the framework (Figures S12 and S13, Supporting Information). Nor are changes observable for the Z7-NS bands, indicating guests are incorporated in a way that does not affect the surrounding host framework. Nano-FTIR (**Figure 4**; Figure S16, Supporting Information) was used to probe the local nanoscale chemical composition of the guest@Z7-NS systems at single points and across 2D fields, with a spatial resolution of ≈20 nm. Near-field vibrational data show the presence of several IR bands, in particular the strong band at 760 cm⁻¹ (corresponding to bIm aromatic ring in-plane and out-of-plane deformations),[61] that align with the Z7-NS nano-FTIR spectra and the corresponding materials' ATR-FTIR spectra. There are, however, no strong bands present that correlate to the spectra of F and RB (Figure 4b,c; Figure S16, Supporting Information). Since nano-FTIR is a surface-based technique, the lack of vibrational modes corresponding to F and RB, indicates the absence of any substantial dye on the surface of the nanosheets, as previous studies in our group have demonstrated.[62] Hence, as the presence of dyes are still observable at a single crystal level by a confocal microscopy (vide infra), this would indicate that the dyes are mainly located within the MOF nanosheets rather than distributed on its surface.

Notably, guest@Z7-NS samples showed negligible dye leaching when suspended in MeOH for 6 months, evincing protected encapsulation in the Z7-NS framework. Moreover, to ensure the presence of the dyes within the nanosheets, we have conducted fluorescence lifetime imaging microscopy (FLIM) experiments for the single guest@Z7-NS samples (Figures S17 and S18, Supporting Information). The FLIM images show a good distribution of the fluorescent dyes over the whole nanosheets, with the emission spectra and decay lifetimes (τ) comparable to that obtained for the bulk samples (vide infra). This local scale characterization unequivocally proves the presence of the dyes in the nanosheet.

2.2. Photophysical Properties

The incorporation of dyes into the Z7-NS host enabled turn-on fluorescence of the guest in the solid state, with no indication of emission from the Z7-NS framework (Figure S19, Supporting Information) or energy transfer between the LMON and guest (**Figure 5**a,b). The emission spectral maps of F@Z7-NS and RB@Z7-NS (Figure S20, Supporting Information) systems exhibit a single emission band characteristic of F and RB. A red shift of the emission is seen with increasing guest loading, resulting in tuneable chromaticity as a function of guest loading (Figure S21, Supporting Information). This is an indication of guest aggregation as shown in other LG@MOFs systems.[46,50]

Excitation spectra and time-resolved photobehaviour obtained through picosecond time-correlated single photon counting (TCSPC) corroborate that guest molecule aggregation is a driver of these luminescent properties (Figure 5c,d; Figure S22 and Tables S2 and S3, Supporting Information). The fluorescence decays (observed at three wavelengths, upon excitation at
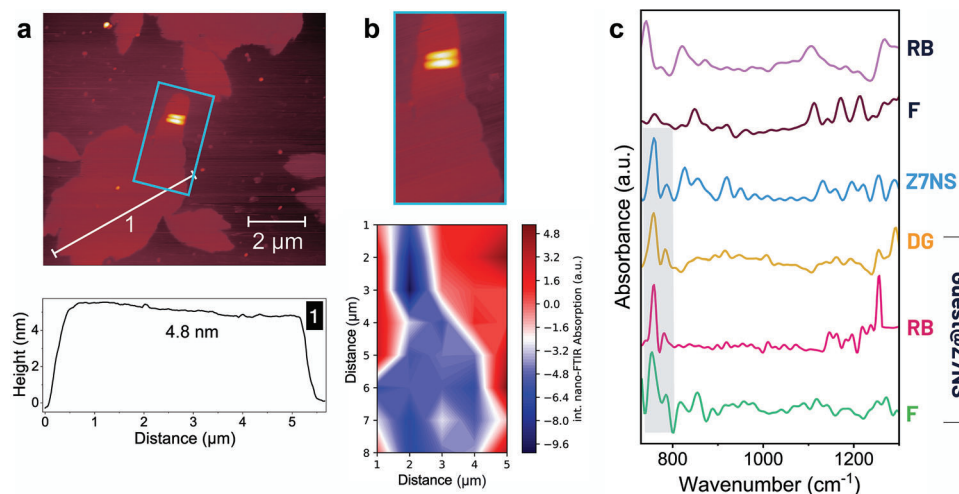
Figure 4. a) AFM topography image (above) of DG@Z7-NS with height profile showing 4.9 nm average height (below) marked by the white line labelled 1 on the image. b) Hyperspectral nano-FTIR imaging across a 2D region of DG@Z7-NS (see in AFM image above) between 725–1271 cm^{-1}. c) Nano-FTIR spectra of various Z7-NS samples.
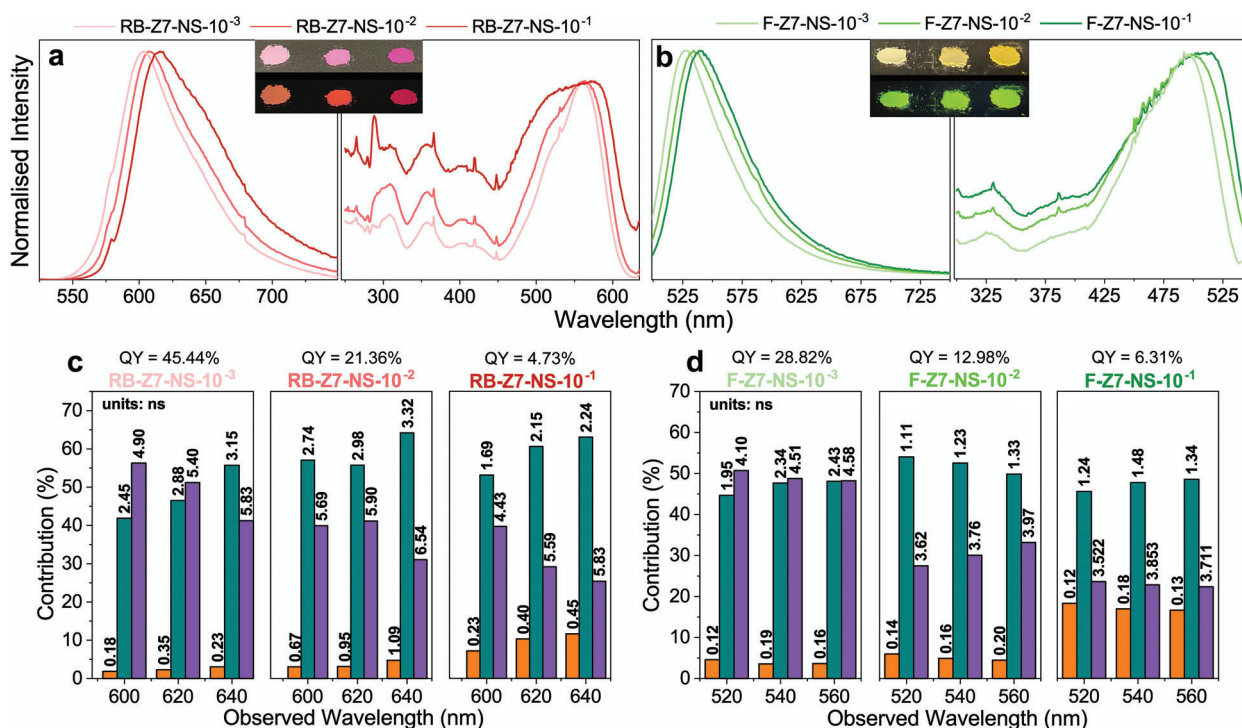
Figure 5. a,b) Emission (left) spectra of guest@Z7 materials excited at 550 nm (RB) and 485 nm (F), and excitation spectra (right) of guest@Z7-NS materials with emission of 650 nm (RB) and 550 nm (F). Inset: powders of guest@Z7-NS-10−3, guest@Z7-NS-10−2 and guest@Z7-NS-10−1 (left-right) under ambient lighting (top) and UV light (bottom). c,d) TCSPC fluorescence lifetime data and photoluminescence quantum yield (QY) of guest@Z7-NS materials across 3 observed wavelengths showing the percentage contribution c on vertical axis and τ values above columns. Orange (τ_1) = H-aggregates, green (τ_2) = J-aggregates, and purple (τ_3) = monomer species.

the maximum of the absorption intensity) of F@Z7-NS and RB@Z7-NS were fitted using a three-component exponential function giving three time constants ($\tau_1 = 0.16$, $\tau_2 = 1.23$, and $\tau_3 = 3.76$ ns for F@Z7-NS at 540 nm; and $\tau_1 = 0.95$, $\tau_2 = 2.98$, and $\tau_3 = 5.90$ ns for RB@Z7-NS at 620 nm) that we assign to H-aggregates (τ_1) (face-to-face), J-aggregates (τ_2) (head-to-tail),

and monomers (τ_3) of F and RB, respectively. Our assignment is based on previous findings for guest@MOF systems and agrees with excitons theory.[49,50,63] Upon increasing concentration of the guest molecules, there is a reduction in contribution of the τ_3-component (monomers), while the τ_2-component (J-aggregates) exhibits minor increase proportional to guest loading. This

observation suggests an increment in J-aggregates population, which is causing a red-shift in the absorption and emission spectra as explained above. On the other hand, τ_1-component (H-aggregates) increases its contribution significantly with the guest loading, reflecting a major formation of H-aggregates. This is further supported by the growth of a shoulder band in the excitation spectrum at higher energies (470 nm for F and 515 nm for RB), and the reduction of PLQY, given emission from H-aggregates is theoretically forbidden.[49,64–66]

These data suggest a mix of monomers and J-aggregates are preferred in dilute guest@Z7-NS samples, likely packing horizontally between the sheets given our structural analysis. With increased guest concentration, more efficient packing between layers leads to aggregation, with H-aggregates being more densely packed. Moreover, our structural analysis revealed the possibility of angular guest stacking and slipped cofacial forms of the J- and H-aggregates are well reported.[65] However, a saturation point appears with RB@Z7-NS-10^{-1} evincing a large increase of H-aggregation. The emission spectra of RB@Z7-NS also present a shoulder ≈650 nm that increases in intensity with higher guest loading, most notably from the 10^{-2} to 10^{-1} samples.

Importantly, we theorize this aggregation occurs in chains, producing long-range order resulting in larger orbitals overlap, as seen in the reduced band gap caused by increasing guest loading (Figure S23, Supporting Information) and reported for other guest@MOF materials.[50] This phenomenon is more pronounced in the RB samples where emission decays are dependent on the gated spectral region, indicative of extended aggregate interactions, likely due to the molecular size of RB. Interestingly, while both RB@Z7-NS and F@Z7-NS exhibit solvatochromism in a range of common organic solvents (Figure S24, Supporting Information), solvatochromic shifts are more pronounced in F@Z7-NS (Figures S25 and S26, Supporting Information). The tighter aggregate packing and molecular size of RB may sterically hinder solvent interactions with RB guests, while in F the looser packing provides interaction sites for sensing, showing selectivity for aprotic solvents (via red-shift of emission) and polar protic solvents (higher emission intensity).

The photostability of these materials was also tested, both exhibiting good performance (Figure S27, Supporting Information). After 24 h of intense exposure to the spectrofluorometer's 150 W xenon bulb irradiating at a wavelength corresponding to each materials absorption maximum, RB@Z7-NS lost 10.5% intensity and F@Z7-NS lost 11.6% but retained chromaticity. 90% of this decrease occurred in the first 10 h, with the following 14 h plateauing to a stable intensity. This loss is comparable to F encapsulated in ZIF-8 reported materials, while F@ZIF-8 materials that exhibited surface aggregation saw over 35% intensity loss after 15 h.[49] This shows a great promise for long-term light-emitting device use of the materials.

2.3. Dual-Guest Emission Mechanism

By intercalating F and RB together in Z7-NS, at a total guest concentration below the determined saturation level for both guests, an optimized warm-yellow emitting material (DG@Z7-NS; DG = F+RB) was synthesized. Luminescence was achieved by exciting the material at the absorption intensity maximum of F

(495 nm), producing an emission spectrum of two distinct but overlapping bands attributable to F (band at 525 nm) and RB (band at 580 nm, **Figure 6**a). The excitation spectra of DG@Z7-NS present two bands with intensity maxima at 495 nm (comparable to the absorption of F) and 560 nm (due to the absorption of RB dye) (Figure 6b; Figure S28, Supporting Information). Remarkably, when the excitation spectrum is recorded at 725 nm (the emission of F dye is barely existent at this wavelength) the band at 495 nm is still observable. Although RB has some absorption cross section at this wavelength, the excitation spectrum of RB@Z7-NS shows that at 495 nm, the signal is decreasing in intensity (Figure 5a; Figure S29, Supporting Information), rather than being a band maximum as for DG@Z7-NS, meaning that this is a new band not detected for RB@Z7-NS. The absorption of F has its maximum intensity at ≈495 nm (Figure 5b; Figure S29, Supporting Information), so it is logical to attribute this new band observed for DG@Z7-NS to the F dye. Additionally, at 725 nm, the excitation spectrum is recorded in a region where RB emits but F does not (Figure 5a,b). This means the excitation spectrum should be similar to the absorption spectrum of RB. However, the spectrum presents as a combination of F and RB. This indicates F is transferring the energy absorbed through photoexcitation to RB for emission in the 725 nm region. This is strong evidence that a Förster resonance energy transfer (FRET) (Figure 6c) exists from the F to RB molecules within the Z7-NS sheets.[67]

Similar behavior has been reported for FRET phenomenon occurring from MOF materials to different guests.[68] Theoretically, energy transfer is possible between F and RB guests due to the spectral overlap of the emission and absorption bands of F and RB, respectively (in the 520–540 nm region) (Figure 6e).[69] FRET is rarely observed between guest dyes in MOF systems, however, due to the lack of proximity between dye molecules, which are typically entrapped within individual pores. The tight space within the MON layers, contrastingly, favors a short distance between guest dyes, triggering the FRET mechanism.[70] Resultingly, the energy absorbed by F upon excitation is partially interconverted to the RB system, from where it is then emitted simultaneously, to produce a yellow emission; the combination of the emission from F monomers not undergoing FRET and RB (Figure 6). To confirm the energy-transfer mechanism, we physically combined F@Z7-NS with RB@Z7-NS in a 1:1 and 10:1 ratio (Figure 6a). The 1:1 ratio powder mixture shows near-yellow emission and, fascinatingly, the emission spectrum aligns with the mathematical superposition of the individual emission spectra of F@Z7-NS and RB@Z7-NS (Figure 6a). In contrast, the emission spectrum for the dual-guest system shows far greater peak overlap, with a shift of the F emission band to longer wavelengths, while the RB emission shifts to shorter ones.

FLIM experiments were also conducted to shed light on the photophysical mechanism of the DG@Z7-NS at a single crystal level. The images of several isolated MONs were collected using two band pass filters (BPF) at 520 ± 20 nm and 623 ± 25 nm to selectively record the emission of F and RB within the MONs, respectively (Figure 6d; Figure S30, Supporting Information). Remarkably, the fluorescence of both dyes is homogenous across the entire Z7-NS, illustrating the homogenous distribution (within the spatial resolution of the microscope, ≈250 nm) of the two guests throughout the ultra-thin nanosheet system. The emission spectra collected at different individual points of these
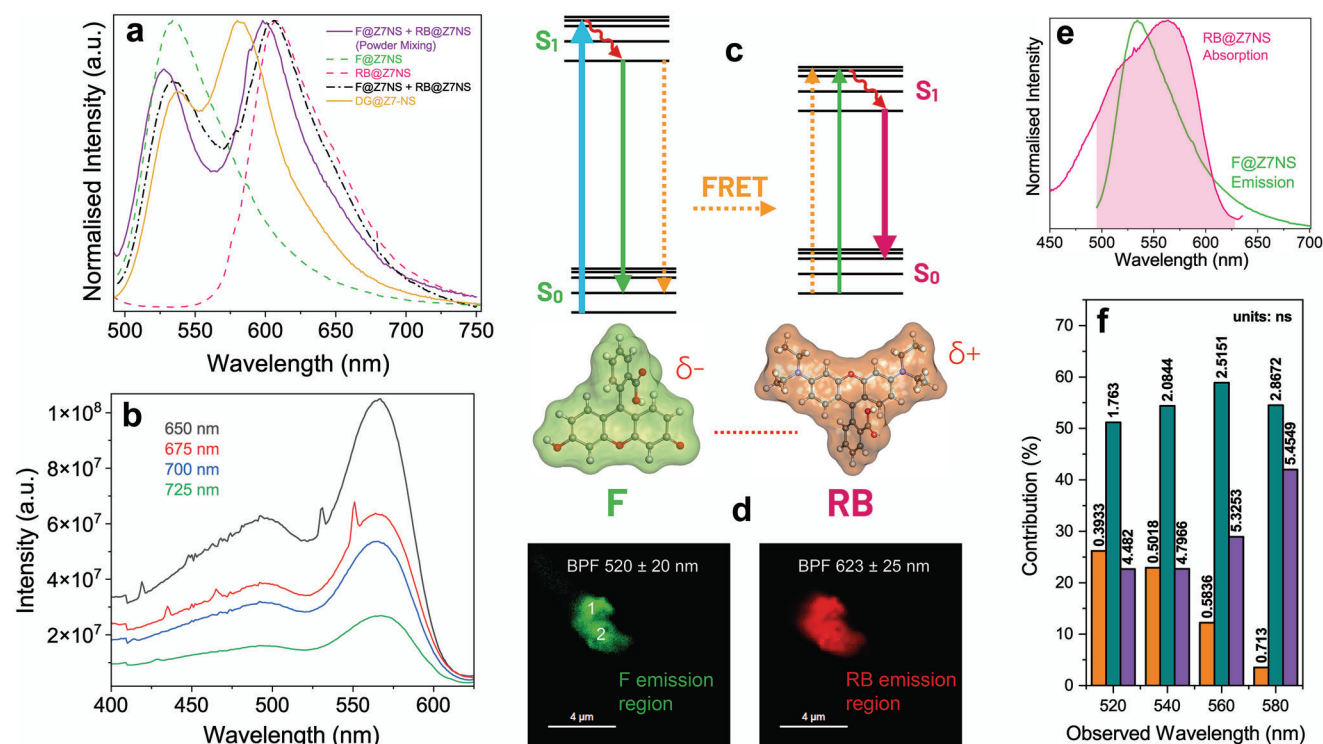
Figure 6. a) Emission spectra of DG@ZIF-7-NS (DG = F+RB) compared to various spectra related to the single-guest F or RB@Z7-NS systems. Black curve indicates mathematical superposition of F@Z7-NS + RB@Z7-NS emission spectra. b) Various excitation spectra of DG@Z7-NS recorded at indicated emission wavelengths. c) Schematic of FRET between F and RB dipole-dipole bound dimers in DG@Z7-NS. d) FLIM of DG@Z7-NS with two band pass filters (BPF) applied (left: 520 ± 20 nm and right 623 ± 25 nm). e) Absorption spectra of RB@Z7-NS overlapped with emission spectra of F@Z7-NS. f) Emission decay lifetimes. Orange (τ_1) = FRET mechanism, green (τ_2) = F, and purple (τ_3) = RB.
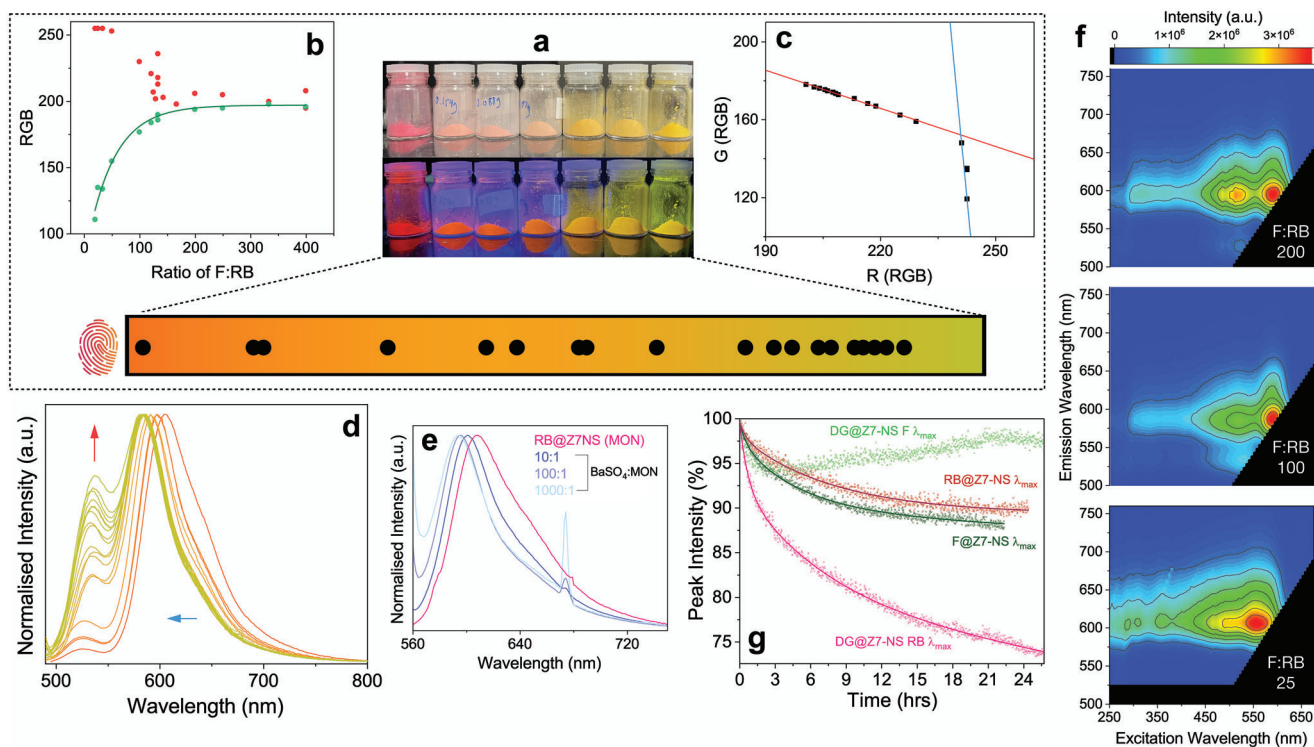
nanosheets closely match with the bulk observation, with two emission bands corresponding to F and RB fluorescence, confirming the phenomena identified in spectrofluorometer measurements, and which are originating from the Z7-NS samples rather than other impurities or crystallized fluorophore mixed phases.

Additionally, the fluorescence decays of bulk DG@Z7-NS were analyzed by a sum of 3-components, assigned as follows: RB (τ_3), F (τ_2) and F-RB coupled FRET mechanism (τ_1) (Figure 6f; Figures S31 and S32, Table S4, Supporting Information). τ_3 and τ_2 are assigned as such for two reasons. This first corresponds with the single-guest system monomer component lifetimes (RB@Z7-NS > F@Z7-NS). The emission lifetime of F in the dual guest system (τ_2) is largely quenched compared to F@Z7-NS, while τ_3 is comparable to RB@Z7-NS, strong evidence of a FRET mechanism. Second, as the observed wavelength varies from the E_{max} of F ($\approx$520 nm) to RB ($\approx$580 nm), the τ_3-component contribution increases significantly, indicating that τ_3 is the lifetime of RB. While at 520 nm RB@Z7-NS shows minimal emission (Figure 6a), the DG@Z7-NS emission spectra (Figure S33, Supporting Information) reveals a hypsochromic shift of the RB band by 30 nm, meaning the RB emission band will exist at 520 nm, allowing τ_3 to still be observable at 520–540 nm. τ_1 is greater than the typical 0.1 ns observed for the H-aggregates of the single-guest Z7-NS systems.[50] Furthermore, the contribution of τ_1 rapidly decreases as the observed wavelength increases, and therefore, it is sensible to attribute this con-

tribution to the FRET mechanism, as it is demonstrated below for the DG@Z7-NS single particles.

The time-resolved photobehavior of the isolated thin films in FLIM also aligns with that of the bulk samples, being the emission decays analyses as a sum of three exponentials (τ_1 = 480–520 ps, τ_2 = 1.8–2.0 ns, and τ_3 = 4.6–5.0 ns when recording at 520 ± 20 nm, and τ_1 = 70–90 ps, τ_2 = 1.9–2.2 ns, and τ_3 = 4.4–5.1 ns when gating at 623 ± 25 nm, Figure S30, Supporting Information). Like our previous attribution, the longest τ_3-component, whose contribution is higher at longer wavelengths (623 ± 25 nm BPF), is assigned to the emission lifetime of the trapped RB dye. On the other hand, the τ_2-component, contributing more at the bluest region, is the emission lifetime of trapped F molecules. Finally, the shortest component is decaying in the highest energetic regions (520 ± 20 nm) but rising (negative amplitude) in the lowest ones (623 ± 25 nm), reflects a FRET from trapped F to RB dyes within the nanosheets. These types of short components decaying in the donor emission region, which become rising components in the acceptor emission region, are typical of photoinduced processes. Since at these wavelengths (623 ± 25 nm) the contribution of F to the signal is much weaker than that of RB, the rise must have its origin from the emission of RB. Hence, we attribute this rising component to the FRET from F to RB, as the photoexcitation of F is populating the excited state of RB. A comparison of the decays obtained from DG@Z7-NS and R@Z7-NS in the RB emission region (BPF of 623 ± 25 nm) (Figure S33, Supporting Information), reinforces this

ADVANCED
SCIENCE NEWS
www.advancedsciencenews.com

ADVANCED
FUNCTIONAL
MATERIALS
www.afm-journal.de

Figure 7. a) Above: selection of synthesised samples in ambient conditions (top) and under UV (bottom), below: predicted finite spectrum of emission chromaticity for DG@Z7-NS derived from correlations, the "emission chromaticity fingerprint", with emission chromaticity of synthesised samples indicated along the spectrum as black dots. b) Correlation between synthesis ratio of F:RB and RGB of emission chromaticity. c) R value of DG@Z7-NS materials correlated with G value (of RGB coordinates, derived from the emission spectra). d) Emission spectra of various DG@Z7-NS samples excited at 470 nm; colours of each spectrum line indicate that sample's emission chromaticity RGB value. e) Emission spectra of RB@Z7-NS when mixed with various ratios of $BaSO_4$. f) Emission-excitation maps of three DG@Z7-NS samples at an F:RB ratio of 25, 100, and 200 (bottom to top). g) Photostability of various guest@Z7-NS samples as a percentage of maximum absorption peak intensity over 24 h with continuous exposure to respective sample Abs_{max}.

finding by presenting a clear rise only in the decay obtained for DG@Z7-NS.

2.4. Tuning the Dual-Guest System

By varying the concentration of F during synthesis of the samples (Table S4 and Figure S28, Supporting Information), a subset of twenty samples of DG@Z7-NS were obtained with distinct emission chromaticity coordinates (**Figure 7**a; Figures S34 and S35, Table S5, Supporting Information). Significantly, the chromaticity of the system can be accurately quantified – allowing for precise fine-tuning of the emission color of DG@Z7-NS. Upon plotting the synthesis ratio of F:RB against the RGB (red-green-blue) values of each sample (Figure 7b), a good logarithmic correlation ($R^2 = 0.997$) was obtained between the F:RB concentration and the G value. Then, when comparing the G value to R value (Figure 7c), we see two clear linear correlations with distinct domains ($R^2 = 0.996$). Together, these data can be used to identify the final emission color of a dual-guest Z7-NS sample based simply on the ratio of F:RB used in the synthetic procedure. If a particular color from green to red is desired, the ratio can be computed using Equations (1) and (2). It is remarkable and of greatest significance is that this relationship confirms that there is only a

discrete subset of colors (a "emission chromaticity fingerprint") attainable by this dual-guest system: those that lie on the two G:R correlations (Figure 7c), seen in the spectrum bar of Figure 7a.

Green value (G)

$$= \frac{80.69604}{\left(1 + 1.29\text{E}^{-4} \times Synthesis\ Ratio\ of\ F:RB\right)^{155.76324}} \quad (1)$$

$$Red\ value\ (R) = \begin{cases} \dfrac{G - 5721}{-22}, & G < 170 \\[2mm] \dfrac{G - 338.15548}{-0.70008}, & G \geq 170 \end{cases} \quad (2)$$

Equations 1 and 2. Quantitative determination of DG@Z7-NS chromaticity based on ratio of F:RB used in the material's synthesis. The empirical coefficients were derived from Figure 7(b) and 7(f) (inset).

The photophysical properties of the dual-guest materials were explored to determine the causes driving these chromaticity findings (Figure 7; Figures S36 and S37, Supporting Information). The spectral changes across the emission spectra of all 20 samples (Figure 7d) also exhibit two clear processes occurring when the concentration of F increases in the system, with high-energy

**ADVANCED
SCIENCE NEWS**

www.advancedsciencenews.com

**ADVANCED
FUNCTIONAL
MATERIALS**

www.afm-journal.de

bands in the excitation spectra vary in similar stages. In the initial phase of 25 to 125 F:RB ratios, there is a blue shift of the RB system along with suppression of a shoulder band identifiable at ≈650 nm. This corresponds to the first steep linear correlation in the R:G chromaticity relationship, with a dramatic increase of F emission with minimal RB value increase. By systematic mixing of the single-guest RB@Z7-NS sample with $BaSO_4$ in increasing ratios as shown in Figure 7e, we suggest that these changes to be a cause of steric hindrance in the system. As the ratio increased from 10:1 to 1000:1, we saw a blueshift of emission peak, and the suppression of a shoulder at ≈650 nm. As more salt crystals were added to RB@Z7-NS, we reasoned that a greater disturbance develops between Z7-NS crystals or even within the layers of sheets in single crystals. This will interfere with long-range interactions that we commented on before and that exists in the RB-Z7 system, particularly the J-aggregates responsible for the shoulder at 650 nm. The result is a general destabilization of the system, and therefore a blue-shifted emission. The same measurement done with F resulted in very minimal shift and spectral shape variance comparably (Figure S38, Supporting Information).

The first process ceases once a ratio of ≈125 is reached, after that the second process dominates: the growth and narrowing of an emission band from F. The change in spectral patterns is most visible when comparing three emission maps (Figure 7f), measured at samples with F:RB ratios of 25, 100 and 200, where a sharpening of emission bands is seen and the growth of a second local maxima at the absorption intensity maxima of fluorescein. Indeed, after the isosbestic point at the R value of 242 in the G:R correlation (Figure 7c) a more subtle linear process also controls this relationship. As shown by the minimal shift from 1000:1 to 100:1 of $BaSO_4$:RB@Z7-NS (Figure 7e), there reaches an equilibrium where steric hindrance no longer affects the energetics. From here, the second process dominates, being the increased emission from fluorescein and the interaction between F and RB molecules as observed in the optimized warm yellow-emitting sample (DG@Z7-NS).

Together, these data reveal that the competitive emission pathways within DG@Z7-NS dictate emission chromaticity. In further support of this are photostability measurements of DG@Z7-NS over 24 h (Figure 7g; Figure S39, Supporting Information). Both guests' decay at rates akin to the single-guest NS systems for the first 3 h, but after the F band begins to intensify as RB continues to diminish. We attribute this to the photodegradation of RB monomers resulting in the reduction of F-RB energy transfer systems. This allows for increased emission from F monomers alone without absorption by RB. This continues until 21.5 h, after that both guests appear to decay at a consistent rate evinced by proportional peak intensity loss in emission spectra. Importantly, always, yellow emission chromaticity is maintained (Figure S39, Supporting Information).

3. Conclusions

This work has demonstrated a new versatile concept for functionalizing 2D MON systems via intercalation of guests. The concept is achieved by the first in situ bottom-up synthesis of Z7-NS using a facile salt-templating methodology. This bottom-up approach produces highly stable, homogenous nanosheets that dispersed without aggregation in solution, and maintain dimensions of a

few-layer thickness (*ca.* 2−3 nm) while extended 5×15 μm² in plane. The selection and trapping of two fluorophores resulted in two single-guest LMONs, both exhibiting strong fluorescence controllable by guest loading concentration that affects guest packing and aggregation. Importantly, the systems show long-term physicochemical stability with a high resistance to leaching. Ultimately, we showed that combining two guests can result in a warm yellow emitting dual-guest intercalated MON that maintains the structural stability and nanosheet morphology of the single-guest systems. The system allows for an enhanced dual-guest energy-transfer interaction and, most remarkably, emission chromaticity that could be quantified so that tuneability became a precisely predictable process. This realization that emission chromaticity is limited to a discrete subset of RGB values presents a strong theoretical foundation for rationally designing future LMON systems. By modelling predicted energetics of the dyes, followed by mapping a sample synthesis, it is possible to design systems of discrete color ranges, with a priori "emission chromaticity fingerprints", ideal for a range of nanophotonic applications from sensing to lighting, layered semi-conductors, product quality assurance and covert security tags.

4. Experimental Section

Synthesis of ZIF-7-III Nanosheets (Z7-NS): $Zn(NO_3)_2$ (59.5 mg, 0.2 mmol) was dissolved in methanol (MeOH) (2 mL). The solution was then added to a conical flask containing NaCl powder (20 g) under vigorous magnetic stirring. After 20 min, benzimidazole (bIm) (283.5 mg, 2.4 mmol) was then dissolved in MeOH (2 mL). The solution was added dropwise to the conical flask followed by vigorous mixing for 12 h. Deionised H_2O (250 mL) was then added to the flask and heated to 100 °C while stirring. The mixture was then siphoned into 50 mL centrifuge tubes and centrifuged at 10000 rpm for 25 min. The collected powder at the bottom of each tube was combined into one tube, followed by further washing and centrifuging cycles (3 × 45 mL H_2O and 5 × 40 mL MeOH). The final product was dried in the tube for 1 h at 90 °C in an oven (≈70%–80% yield).

Samples characterized by AFM, nano-FTIR, FE-SEM and TEM were prepared by adding 5 mg of Z7-NS in a vial with 10 mL of MeOH. The vial was sonicated for 1 min to disperse the Z7-NS before drop casting the solution onto the sample substrate. To obtain particle size separation, after 24 h, the solution was pipetted from the centre or base of the vial depending on preferred particle morphology.

Synthesis of Guests@Z7-NS Materials: The synthesis above was repeated except that initially Fluorescein (F) or Rhodamine B (RB) (0.003 mmol, 0.0003 mmol or 0.03 mmol) were solubilized with MeOH (2 mL) via sonication. This solution was mixed with the bIm solution before then adding to the $Zn(NO_3)_2$@NaCl vial.

Synthesis of ZIF-7-III: ZIF-7-III was synthesized via an adapted protocol by Peng et al.[33] Synthesis of ZIF-7 (I): DMF (100 mL) was added to a mixture of $Zn(NO_3)_2 \cdot 6H_2O$ (303 mg) and bIm (770 mg). After stirring for 1 h, the solution was kept at room temperature for 96 h. The formed ZIF-7 crystals were collected by centrifugation and washed with MeOH (5×50 mL). The wet product was dried at 50 °C for 8 h and then at 120 °C for 48 h in a vacuum oven.

ZIF-7-III: the obtained ZIF-7 crystals were dispersed in distilled water at a concentration of 0.5 wt.% and then refluxed at 100 °C for 24 h. The resulting turbid dispersion was filtered and washed with distilled water (3×50 mL) and MeOH (4×50 mL). The product was dried at 50 °C for 12 h to form the layered product $Zn_2(bim)_4$.

Powder X-Ray Diffraction: Powder x-ray diffraction (PXRD) patterns were collected using a Rigaku MiniFlex diffractometer equipped with a Cu Kα source and step size of 0.0025° at a scan rate of 0.04° min⁻¹. Sam-

ples were prepared using a 0.1 mm shallow well sample holder. High-resolution XRD patterns were collected at the Diamond Light Source I11 beamline using the MAC detection system. Calibrations were performed using Si powder standard (NIST SRM640c), with an X-ray beam energy of 15 keV (0.826834(10) Å) and scan time of 3600 s. Samples were prepared in borosilicate glass capillaries of 0.5 mm diameter. d-spacing was calculated using Bragg's Law.

Attenuated Total Reflectance Fourier Transform Infrared Spectroscopy: Attenuated Total Reflectance Fourier Transform Infrared Spectroscopy (ATR-FTIR) measurements of bulk Z7 and Z7-NS materials were performed using a Nicolet iS10 FTIR spectrometer. High-resolution synchrotron radiation infrared (SR-IR) measurements of the mid-IR and far-IR (FIR) spectra were performed at the Diamond Light Source B22 MIRIAM beamline. FIR and MIR spectra were collected under vacuum, using the ATR module installed on the Bruker Vertex 80 V FTIR bench equipped with the DLaTGS detector. For improved signal-to-noise ratio, liquid helium-cooled bolometer was used in FIR measurements.

Nano-FTIR: Near-field optical measurements were collected using the neaSNOM instrument (neaspec GmbH) based on a tapping-mode AFM. The platinum-coated tip (NanoAndMore GmbH, cantilever resonance frequency 250 kHz and nominal tip radius ≈20 nm) was illuminated by a Toptica broadband mid-infrared (MIR) femtosecond laser. Individual crystals of Z7 and Z7-NS type materials were analyzed by averaging 4 measurements with 18 individual point spectra each. For each sample, at least 10 unique crystals or regions were probed. Each spectrum was acquired from an average of 20 Fourier-processed interferograms with 10 cm^{-1} spectral resolution, 2048 points per interferogram, and an 18-ms integration time. The sample spectrum was normalized to a reference spectrum measured on a silicon surface to reconstruct the final nano-FTIR amplitude and phase. The continuous broadband MIR spectra were attained by combining two illumination sources, then the obtained spectra were combined at 1500 cm^{-1}. All measurements were carried out under ambient conditions (≈40% RH).

Raman Spectroscopy: Raman spectra were collected using the Bruker MultiRAM Raman spectrometer with sample compartment D418, equipped with a Nd-YAGlaser (1064 nm) and a LN-Ge diode as a detector. The laser power used for sample excitation was 50 mW, and 64 scans were accumulated at a resolution of 1 cm^{-1}.

Thermogravimetric Analysis: Thermogravimetric analysis (TGA) was performed using a TA Instruments Q50 TGA machine equipped with a platinum sample holder under an N_2 inert atmosphere at a heating rate of 10°C min^{-1} from 30 to 800 °C.

Atomic Force Microscopy: Atomic force microscopy (AFM) imaging was performed with a neaSNOM instrument (neaspec GmbH) operating in tapping mode. Height topography images were collected using the Scout350 probe (NuNano), which has a nominal tip radius of 5 nm, a spring constant of 42 N m^{-1} and resonant frequency of 350 kHz.

Scanning Electron Microscopy: Backscattered electron and secondary electron scanning electron microscopy (SEM) images were obtained at 10 keV under high vacuum using a SEM Tescan Lyra 3 (Tescan, Czech Republic) with secondary and backscattered electron imaging (SEI and BSE respectively) using a voltage from 10 to 15 keV. Samples were drop cast onto silicon wafer or a polished aluminium specimen stub that was coated with gold (Au) with a thickness of 25 nm using SC7620 sputter coater (Quorum Technologies) at 20 mA plasma current for 3 min.

Spectrofluorimetric Measurements: Steady–state fluorescence spectra, steady–state diffuse reflectance spectra, photoluminescence quantum yield (PLQY), and TCSPC emission decay data were recorded using the FS-5 spectrofluorometer (Edinburgh Instruments) equipped with the appropriate modules for each specific experiment. For TCSPC measurements, the samples were pumped with a 365 nm EPLED picosecond pulsed laser source. Lifetime fitting of the time constants from decay data was performed using the Fluoracle software. Excitation spectra exhibit artefacts (sharp peaks) from equipment operation that were not removed in presented data.

Fluorescence Lifetime Imaging: Fluorescence lifetime images (FLIM) were recorded using an inverted-type scanning confocal fluorescence microscope (MicroTime-200, Picoquant, Berlin) with a 60× NA1.2 Olympus water immersion objective, and a 2D piezo scanner (Physik Instrumente). A 470-nm pulsed diode laser (pulse width ≈40 ps) was employed as the excitation source. A dichroic mirror (AHF, Z375RDC), a 500-nm long-pass filter (AHF, HQ500lp), a 100-μm pinhole, and an avalanche photodiode detector (MPD, PDM series) were used to collect the emission. Moreover, the FLIM and emission decays of the DG@Z7-NS sample were collected using two band pass filters (520 ± 20 and 623 ± 25 nm) to selectively record the emission region of F and RB, respectively. The emission spectrum was recorded using a spectrograph (Andor SR 303i-B) equipped with a 1600×200 pixels EMCCD detector (Andor Newton DU-970N-BV) coupled to the Micro-Time-200 system.

Transmission Electron Microscopy: Transmission electron microscopy (TEM) characterization was performed at 200 keV accelerating voltage using a LaB$_6$ electron source using a JEM-2100 electron microscope. The images were recorded on a Gatan Orius camera through Digital Micrograph.

Nuclear Magnetic Resonance Guest Loading Analysis: Samples for nuclear magnetic resonance (NMR) were dissolved in a solution composed of 500 μL methanol-d4 and 50 μL DCl/D$_2$O (35 wt.%). All NMR spectroscopy was done at 298 K using a Bruker AvanceIII spectrometer operating at 600 MHz, equipped with a BBO cryoprobe. Data were collected using a relaxation delay of 20 s, with 128 k points and a sweep width of 19.8 ppm, giving a digital resolution of 0.18 Hz. Data was processed using Bruker Topspin with a line broadening of 1 Hz and 2 rounds of zero-filling. The loading amount was calculated from the molar ratio of compound to bIm. To calculate the molar ratio, peaks corresponding to each compound were integrated and normalized according to the number of protons giving rise to the signal. For fluorescein (F), the doublet at ≈8.30 ppm was used, which corresponds to a single proton (that in the ortho position relative to the carboxyl group). For Rhodamine B (RB) the broad multiplet at ≈8.22 ppm was used, which corresponds to the equivalent single proton in the ortho position relative to the carboxyl group. For benzimidazole the singlet at ≈9.33 ppm was used, which corresponds to the single proton of the imidazole group, adjacent to the two nitrogens. Global spectral deconvolution (in the MestReNova software package) was used to pick and integrate the peaks.

Supporting Information

Supporting Information is available from the Wiley Online Library or from the author.

Conflict of Interest

The authors declare no conflict of interest.

Author Contributions

Conceptualization was done by D.S and J.-C.T. Methodology was developed by D.S. Synthesis was performed by D.S. AFM, PXRD, nano-FTIR, FIR, MIR and FS-5 spectrofluorimetric measurements were performed by D.A.S. SEM characterization was performed by C.B. and D.S. TEM characterization was performed by I.G. with analysis of the data by D.A.S. FLIM experiments were performed and analyzed by M.G. and A.D. NMR was performed by N.A. TGA, band gap and Raman data was collected by S.M, analysis performed by D.A.S. Manuscript was drafted by D.A.S, with review and editing by D.A.S., M.G., A.D. and J.-C.T. Supervision by J.-C.T.

Data Availability Statement

The data that support the findings of this study are available in the supplementary material of this article.

Keywords

[1] J. Nicks, K. Sasitharan, R. R. R. Prasad, D. J. Ashworth, J. A. Foster, *Adv. Funct. Mater.* **2021**, *31*, 2103723.
[2] D. J. Ashworth, J. A. Foster, *J. Mater. Chem. A* **2018**, *6*, 16292.
[3] M. Zhao, Y. Huang, Y. Peng, Z. Huang, Q. Ma, H. Zhang, *Chem. Soc. Rev.* **2018**, *47*, 6267.
[4] N. K. Chaudhari, H. Jin, B. Kim, D. San Baek, S. H. Joo, K. Lee, *J. Mater. Chem. A* **2017**, *5*, 24564.
[5] H. Yin, Z. Tang, *Chem. Soc. Rev.* **2016**, *45*, 4873.
[6] W.-J. Ong, L.-L. Tan, Y. H. Ng, S.-T. Yong, S.-P. Chai, *Chem. Rev.* **2016**, *116*, 7159.
[7] C. Tan, X. Cao, X. J. Wu, Q. He, J. Yang, X. Zhang, J. Chen, W. Zhao, S. Han, G. H. Nam, M. Sindoro, H. Zhang, *Chem. Rev.* **2017**, *117*, 6225.
[8] J. C. Tan, P. J. Saines, E. G. Bithell, A. K. Cheetham, *ACS Nano* **2012**, *6*, 615.
[9] Z. Zeng, I. S. Flyagina, J.-C. Tan, *Nanoscale Adv* **2020**, *2*, 5181.
[10] Y. Peng, W. Yang, *Adv. Mater. Interfaces* **2019**, *7*, 1901514.
[11] X. Chen, T. Zhang, S. Liu, H. Wen, L. Chen, *IOP Conf. Ser.: Earth Environ. Sci.* **2018**, *170*, 052040.
[12] J. Liu, X. Song, T. Zhang, S. Liu, H. Wen, L. Chen, *Angew Chem Int Ed Engl* **2020**, *60*, 5612.
[13] H. L. Zhu, D. X. Liu, *J. Mater. Chem. A* **2019**, *7*, 21004.
[14] D. Zhu, M. Qiao, J. Liu, T. Tao, C. Guo, *J. Mater. Chem. A* **2020**, *8*, 8143.
[15] C. Tan, G. Liu, H. Li, Y. Cui, Y. Liu, *Dalton Trans.* **2020**, *49*, 11073.
[16] Y. Peng, W. Yang, *Sci China Chem* **2019**, *62*, 1561.
[17] R. Banerjee, A. Phan, B. Wang, C. Knobler, H. Furukawa, M. O'Keeffe, O. M. Yaghi, *Science* **2008**, *319*, 939.
[18] Q.-F. Yang, X.-B. Cui, J.-H. Yu, J. Lu, X.-Y. Yu, X. Zhang, J.-Q. Xu, Q. Hou, T.-G. Wang, *CrystEngComm* **2008**, *10*, 1534.
[19] P. Zhao, G. I. Lampronti, G. O. Lloyd, M. T. Wharmby, S. Facq, A. K. Cheetham, S. A. Redfern, *Chem. Mater.* **2014**, *26*, 1767.
[20] H. L. Liu, Y. J. Chang, T. Fan, Z. Y. Gu, *Chem. Commun.* **2016**, *52*, 12984.
[21] Y. Peng, Y. Li, Y. Ban, W. Yang, *Angew. Chem. Int. Ed. Engl.* **2017**, *56*, 9757.
[22] W. M. Liao, J. H. Zhang, S. Y. Yin, H. Lin, X. Zhang, J. Wang, H. P. Wang, K. Wu, Z. Wang, Y. N. Fan, M. Pan, C. Y. Su, *Nat. Commun.* **2018**, *9*, 2401.
[23] N. Contreras-Pereda, P. Hayati, S. Suarez-Garcia, L. Esrafili, P. Retailleau, S. Benmansour, F. Novio, A. Morsali, D. Ruiz-Molina, *Ultrason. Sonochem.* **2019**, *55*, 186.
[24] Y. Fan, J. Zhang, Y. Shen, B. Zheng, W. Zhang, F. Huo, *Nano Res.* **2021**, *14*, 1.
[25] Y. Zhao, L. Jiang, L. Shangguan, L. Mi, A. Liu, S. Liu, *J. Mater. Chem. A* **2018**, *6*, 2828.
[26] Z. Hu, E. M. Mahdi, Y. Peng, Y. Qian, B. Zhang, N. Yan, D. Yuan, J.-C. Tan, D. Zhao, *J. Mater. Chem. A* **2017**, *5*, 8954.
[27] T. Rodenas, I. Luz, G. Prieto, B. Seoane, H. Miro, A. Corma, F. Kapteijn, I. X. F. X. Llabres, J. Gascon, *Nat. Mater.* **2015**, *14*, 48.
[28] S. C. Junggeburth, L. Diehl, S. Werner, V. Duppel, W. Sigle, B. V. Lotsch, *J. Am. Chem. Soc.* **2013**, *135*, 6157.
[29] M. Zhao, Y. Wang, Q. Ma, Y. Huang, X. Zhang, J. Ping, Z. Zhang, Q. Lu, Y. Yu, H. Xu, Y. Zhao, H. Zhang, *Adv. Mater.* **2015**, *27*, 7372.
[30] L. Huang, X. Zhang, Y. Han, Q. Wang, Y. Fang, S. Dong, *J. Mater. Chem. A* **2017**, *5*, 18610.
[31] K. Zhao, S. Liu, G. Ye, X. Wei, Y. Su, W. Zhu, Z. Zhou, Z. He, *Chem. Sus. Chem.* **2020**, *13*, 1556.
[32] D. Liu, B. Liu, C. Wang, W. Jin, Q. Zha, G. Shi, D. Wang, X. Sang, C. Ni, *ACS Sustainable Chem. Eng.* **2020**, *8*, 2167.
[33] Y. Peng, Y. S. Li, Y. J. Ban, H. Jin, W. M. Jiao, X. L. Liu, W. S. Yang, *Science* **2014**, *346*, 1356.
[34] L. Huang, Z. Hu, H. Jin, J. Wu, K. Liu, Z. Xu, J. Wan, H. Zhou, J. Duan, B. Hu, J. Zhou, *Adv. Funct. Mater.* **2020**, *30*, 1908486.
[35] B. Yan, W. Zhang, X. Qin, Y. Choi, G. Diao, X. Jin, Y. Piao, *Chem. Eng. J.* **2020**, *400*, 125895.
[36] Q. Q. Xia, X. H. Wang, J. L. Yu, Z. Y. Xue, J. Chai, M.-X. Wu, X. Liu, *Dalton Trans.* **2022**, *51*, 9397.
[37] Z. J. Li, X. Y. Li, Y. T. Yan, L. Hou, W. Y. Zhang, Y. Y. Wang, *Cryst. Growth Des.* **2018**, *18*, 2031.
[38] M. D. Allendorf, C. A. Bauer, R. K. Bhakta, R. J. T. Houk, *Chem. Soc. Rev.* **2009**, *38*, 1330.
[39] H. Xu, J. Gao, X. Qian, J. Wang, H. He, Y. Cui, Y. Yang, Z. Wang, G. Qian, *J. Mater. Chem. A* **2016**, *4*, 10900.
[40] R. A. Natour, Z. K. Ali, A. Assoud, M. Hmadeh, *Inorg. Chem.* **2019**, *58*, 10912.
[41] W. W. Zhao, J. L. Peng, W. K. Wang, S. J. Liu, Q. Zhao, W. Huang, *Coord. Chem. Rev.* **2018**, *377*, 44.
[42] Q. Jiang, C. Zhou, H. Meng, Y. Han, X. Shi, C. Zhan, R. Zhang, *J. Mater. Chem. A* **2020**, *8*, 15271.
[43] Y. Zhu, X. Sun, Y. Tang, L. Fu, Y. Lu, *Nano Res.* **2020**, *14*, 1912.
[44] J. Tang, Z. Liang, M. Huang, S. Su, Y. Wen, Q.-L. Zhu, X. Wu, *J. Mater. Chem. C* **2021**, *9*, 14628.
[45] B. B. Guo, J. C. Yin, N. Li, Z. X. Fu, X. Han, J. Xu, X. H. Bu, *Adv. Opt. Mater.* **2021**, *9*, 2100283.
[46] M. Gutierrez, Y. Zhang, J. C. Tan, *Chem. Rev.* **2022**, *122*, 10438.
[47] M. J. T. Snare, F. E. Treloar, K. P. Ghiggino, P. J. Thistlethwaite, *J. Photochem.* **1982**, *18*, 335.
[48] R. N. Sjöback, J. Nygren, M. Kunista, *Spectrochim. Acta* **1995**, *51*, L7.
[49] T. Xiong, Y. Zhang, L. Donà, M. Gutiérrez, A. F. Möslein, A. S. Babal, N. Amin, B. Civalleri, J.-C. Tan, *ACS Appl. Nano Mater.* **2021**, *4*, 10321.
[50] Y. Zhang, M. Gutierrez, A. K. Chaudhari, J. C. Tan, *ACS Appl. Mater. Interfaces* **2020**, *12*, 37477.
[51] A. K. Chaudhari, J. C. Tan, *Adv. Opt. Mater.* **2020**, *8*, 1901912.
[52] A. K. Chaudhari, H. J. Kim, I. Han, J. C. Tan, *Adv. Mater.* **2017**, *29*, 1701463.
[53] R. Xu, Y. Wang, X. Duan, K. Lu, D. Micheroni, A. Hu, W. Lin, *J. Am. Chem. Soc.* **2016**, *138*, 2158.
[54] C. He, K. Lu, W. Lin, *J. Am. Chem. Soc.* **2014**, *136*, 12253.

ADVANCED
SCIENCE NEWS

www.advancedsciencenews.com

ADVANCED
FUNCTIONAL
MATERIALS

www.afm-journal.de

[55] D. Saliba, M. Al-Ghoul, *Philos. Trans. A Math Phys. Eng. Sci.* **2016**, *374*, 20160138.

[56] U. Riaz, S. M. Ashraf, S. Kumar Saroj, M. Zeeshan, S. Jadoun, *RSC Adv.* **2016**, *6*, 34534.

[57] R. Gao, D. Yan, X. Duan, *Cell Rep. Phys. Sci.* **2021**, *2*, 100536.

[58] M. Hirose, F. Ito, T. Shimada, S. Takagi, R. Sasai, T. Okada, *Langmuir* **2017**, *33*, 13515.

[59] X. Xiao, H. Song, S. Lin, Y. Zhou, X. Zhan, Z. Hu, Q. Zhang, J. Sun, B. Yang, T. Li, L. Jiao, J. Zhou, J. Tang, Y. Gogotsi, *Nat. Commun.* **2016**, *7*, 11296.

[60] Y. Zhang, Z. Teng, Q. Ni, J. Tao, X. Cao, Y. Wen, L. Wu, C. Fang, B. Wan, X. Zhang, G. Lu, *ACS Appl. Mater. Interfaces* **2020**, *12*, 57810.

[61] M. R. Ryder, B. Civalleri, T. D. Bennett, S. Henke, S. Rudic, G. Cinque, F. Fernandez-Alonso, J. C. Tan, *Phys. Rev. Lett.* **2014**, *113*, 215502.

[62] A. F. Möslein, M. Gutierrez, B. Cohen, J. C. Tan, *Nano Lett.* **2020**, *20*, 7446.

[63] M. Kasha, *Discuss. Faraday Soc.* **1950**, *9*, 14.

[64] B. Heyne, *Photochem. Photobiol. Sci.* **2016**, *15*, 1103.

[65] N. J. Hestand, F. C. Spano, *Chem. Rev.* **2018**, *118*, 7069.

[66] D. Setiawan, A. Kazaryan, M. A. Martoprawiro, M. Filtaov, *Phys. Chem. Chem. Phys.* **2010**, *12*, 11238.

[67] T. Förster, *Ann. Phys.* **1948**, *437*, 55.

[68] M. Gutiérrez, F. Sáncheze, A. Douhal, *J. Mater. Chem. C* **2015**, *3*, 11300.

[69] J.-X. Wang, J. Yin, O. Shekhah, O. M. Bakr, M. Eddaoudi, O. F. Mohammed, *ACS Appl. Mater. Interfaces* **2022**, *14*, 9970.

[70] H. Sahoo, *J Photochem Photobiol* **2011**, *12*, 20.

2214307 (13 of 13)